Journal of Materials Science: Materials in Electronics
https://doi.org/10.1007/s10854-019-00787-2

Field emission investigations of solvothermal synthesized and soaked rutile-TiO_2 nanostructures

Ajinkya Bhorde[1] · Somnath Bhopale[2] · Ravindra Waykar[1] · Shruthi Nair[1] · Haribhau Borate[1] · Subhash Pandharkar[1] · Adinath Funde[1] · Mahendra More[2] · Sandesh Jadkar[2]

Received: 4 July 2018 / Accepted: 22 January 2019

Abstract
In present work we report synthesis of rutile-TiO_2 by using a simple solvothermal method. The formation of pure single phase rutile-TiO_2 has been confirmed by X-ray diffraction (XRD) and Raman spectroscopy analysis. The XRD analysis revealed that as-prepared and soaked-TiO_2 has pure rutile phase with tetragonal crystal structure. The field emission scanning electron microscopy and high resolution transmission electron microscopy analysis shows that as-prepared TiO_2 has nano-rods like morphology whereas soaked-TiO_2 has nano-flowers like morphology with atomically sharp edges. The UV–Visible spectroscopy analysis showed that as-prepared and soaked rutile-TiO_2 nano-structures have absorption edge in the visible range and having band gap of ~ 3.58 eV. The field emission (FE) properties of as-prepared and soaked rutile-TiO_2 nano-structures were investigated and it was observed that as-prepared and soaked rutile-TiO_2 display excellent FE properties with low turn-on field (~ 4.8 V/μm for 10 μA/cm^2), maximum current density [~ 444 μA/cm^2 (as-prepared) and 508 μA/cm^2 (soaked)] and superior current stability (~ 3 h for ~ 1 μA). The obtained results show that the rutile-TiO_2 nanostructures can be useful for practical applications in vacuum nano/microelectronic devices.

1 Introduction

Compared to the other 1D metal oxide nano-materials such as zinc oxide (ZnO) [1], tin oxide (SnO_2) [2], tungsten oxide (WO_3) [3], iron oxide (Fe_2O_3) [4] etc. the titanium dioxide (TiO_2) has received considerable attention for applications in solar cells [5], catalysis [6], photo-catalysis [7], electrochromic displays [8], super capacitors [9], batteries [10], gas sensing [11], environmental purification [12], photonic crystals [13], biological templates [14], solar cells [15] etc. due to its excellent chemical, optical and mechanical properties, non-toxicity, abundance, low cost, and good thermal and chemical stability. It occurs in three different crystalline phases namely rutile (tetragonal), brookite (orthorhombic) and anatase (tetragonal) [16]. Anatase and brookite phases are metastable while rutile is thermodynamically most stable phase. The synthesis of Brookite phase is much more difficult as compare the synthesis of anatse and rutile phase TiO_2 and is available as a natural single crystal [17]. Various methods are generally used for the preparation of TiO_2 nanostructures which includes chemical vapor deposition (CVD) [18], Solvothermal [19], sol–gel [20], spin coating [21], electro spinning [22], sonochemical synthesis [23] and inverse microemulsion method [24], anodization [25] etc. Among these, Solvothermal method has several advantages such as requirement of low cost precursors, environmental safely due to closed reaction process, low temperature process so better control on stoichiometric, it has ability to control particle size and morphology of synthesized material by controlling different process parameters. Furthermore, it can be mix-up with other processes such as optical radiation, hot-pressing, ultrasound, microwave, and electrochemistry etc. for reaction kinetics enhancement. Solvothermal synthesis method also has the merit of rapid growth rates due to the rapid diffusion processes. However, the method has few limitations such as safety issues during the reaction process, need of costly autoclaves and impossibility of observing the reaction process etc. [26].

The anatase-to-pure rutile transformation (ART) of TiO_2 is envisaged as a transformation from a metastable state to stable state. In solvothermal method the phase

✉ Sandesh Jadkar
sandesh@physics.unipune.ac.in

[1] School of Energy Studies, Savitribai Phule Pune University, Pune 411 007, India

[2] Department of Physics, Savitribai Phule Pune University, Pune 411 007, India

Published online: 31 January 2019

transformation is critically dependent on post-annealing or calcination temperature, pressure, particle size, impurities, additives/dopants, and solvothermal conditions. It has been reported that high process temperature has been needed for ART. For example Li et al. [27]. reported a temperature range of 700–800 °C whereas Jagtap et al. [28] obtained the onset of transformation temperature by subjecting anatase-TiO_2 to heat treatment from 150 to 950 °C. However, no unique phase transformation temperature is reported. The high process temperature also limits its potential application in device fabrication. With this stimulation an attempt has been made to prepare nano-structured pure phase rutile-TiO_2 from anatase-TiO_2 powder precursor using simple solvothermal method at low temperature (~ 200 °C). Formation of rutile-TiO_2 powder has been verified by X-ray diffraction (XRD) and micro- raman spectroscopy analysis. Furthermore, formation of nano-structure rutile-TiO_2 powder has been confirmed by field emission scanning electron microscopy and transmission electron microscopy. Finally, the field emission properties of nano-structure rutile-TiO_2 powder were examined in view of its application for large-area emitters.

2 Experimental

2.1 Synthesis and growth mechanism of rutile-TiO_2 nanostructures

In the present study rutile-TiO_2 powder has been synthesized by using simple solvothermal method. For synthesis anatase-TiO_2 powder and Sodium Hydroxide (NaOH) (both Thomas Baker, India) were used directly without any further purification. A Teflon linear autoclave was cleaned by simple chemical process using sulfuric acid (H_2SO_4) and hydrochloric acid (HCl). 1 gm anatase-TiO_2 added directly in 10 M NaOH (18 ml of volume). After sonication for 15 min resultant solution was transferred into stainless steel autoclave, Teflon lined pot containing resultant solution with its 80% of total volume and kept at constant temperature, 200 °C in muffle furnace for 16 h. After completing 16 h time the stainless steel autoclave was air cooled to ambient temperature. The resulting white precipitate was then washed several times with distilled water until the pH become ~ 7 and dried at 60 °C for 2 h. The resulting precipitate further transferred for acid treatment, which involved stirring in 0.1 M HCl solution for 12 h. Then washed thoroughly with water and subsequently air-dried at 80 °C over night to obtain the TiO_2 precursor (as-prepared rutile-TiO_2).The same precipitate soaked as it is for 5 days in double distilled water by maintaining pH ~ 7. After that the precipitate dried in air at 60 °C for 2 h. Then washed thoroughly with water and subsequently air-dried at 80 °C over night to obtain the TiO_2 precursor (soaked rutile-TiO_2). Figure 1 shows the flow chart of as-prepared and soaked rutile-TiO_2 powder.

The ART is a nucleation and growth process and the kinetics of this transition depends on impurities, morphology, sample preparation method, heat flow conditions, etc. [29]. The ART has been widely studied for both scientific and application-driven reasons because the TiO_2 phase is one of the critical factors for many applications. The possible reaction mechanism of formation of rutile-TiO_2 from its anatase phase in solvothermal method is as follows;

At the first step, high concentrated NaOH (10 M, alkaline solution) reacted with anatase-TiO_2 powder at temperature 200 °C for 16 h to form sodium metatitanate ($Na_2Ti_3O_7$) in an autoclave via reaction [30].

$$3\,TiO_2 + 2\,NaOH \rightarrow Na_2Ti_3O_7 + H_2O \quad (1)$$

During the hydrothermal treatment some Ti–O–Ti bonds of the TiO_2 precursor break and thermodynamically unstable six-coordinated monomers $[Ti(OH)_6]_2$ are formed and saturated. These monomers become stable when their size exceeds certain nuclei size [31]. The unstability of sodium metatitanate can be prevented by washing the white slurry solution with de-ionised water and followed by acid solution HCl until pH 7. The ion exchange between Na^+ and H^+ occurs during the acid wash treatment and hydrogenotitanate ($H_2Ti_3O_7$) forms. The chemical reaction can be described as [31].

$$Na_2Ti_3O_7 + 2\,HCl \rightarrow H_2Ti_3O_7 + 2\,NaCl \quad (2)$$

The acid washing process influences the formation of nanotubes and the hydrothermal treatment affects their structural composition [32]. Wang et al. [33] found that the acid washing process determine the morphology, length and other properties of nanotubes such as composition, annealing characteristics, and specific surface.

Finally, the dehydration process of powder at 80 °C for 12 h causes crystal lattice rearrangement to form rutile-TiO_2 via reaction.

$$H_2Ti_3O_7 \rightarrow 3TiO_2 + H_2O \quad (3)$$

The most acceptable mechanism for anatase-to-rutile phase transformation was proposed by Shanon et al. [34] and developed by Banfield and his group [35]. Banfield et al. suggested that the aggregation of nano-crystal anatase played the most important role in anatase-to-rutile phase transformation process. According to them anatase twin boundaries are constructed from structural elements and these twin interfaces can be regarded as the nuclei of rutile phase. Such interface nucleation has the lowest activation barriers for rutile nucleation. This mechanism is applicable for both calcination-induced and hydrothermal-treatment-mediated phase transformation from anatase-to-rutile. Under the hydrothermal condition, the nanostructured TiO_2 showed

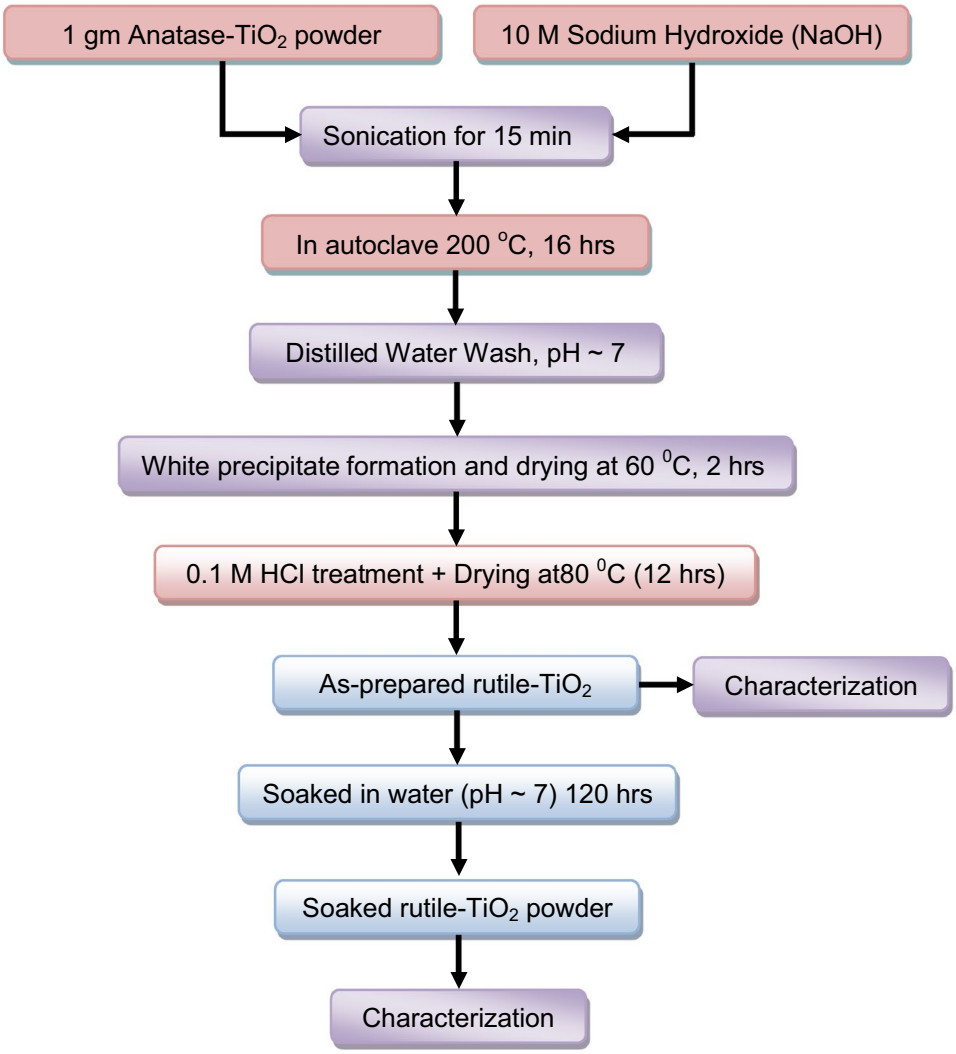

Fig. 1 Process flow chart of preparation of as-prepared rutile-TiO_2 and soaked rutile-TiO_2 powder

higher mobility, and they can adjust their orientations even after aggregation to achieve a more thermodynamically stable state [36]. Additionally, the surface atoms are easier to rearrange, which reduces further the energy barrier for nucleation and thus facilitated the growth of rutile-TiO_2 phase [37].

2.2 Material characterization

X-ray diffraction pattern were obtained by using X-ray diffractometer (Bruker D8 Advance, Germany) using CuKα line ($\lambda = 1.54056$ Å). The optical band gap and reflectance of rutile-TiO_2 powder was deduced from diffused reflectance spectra (DRS) and was measured using a JASCO, V-670 UV–Visible spectrophotometer in the range of 200–750 nm. The field emission scanning electron microscopy (FE-SEM) images were captured using Hitachi, S-4800, Japan with operating voltage 10 kV to study the surface morphology of synthesized samples. High resolution transmission electron micrographs (HR-TEM) and selected area electron diffraction (SAED) patterns were obtained using TECNAI G^2-20-TWIN transmission electron microscope operating at 200 kV. Raman spectra were recorded using Raman spectroscopy (Renishaw In Via microscope Raman) in the range of 100–650 cm^{-1}. The spectrometer has backscattering geometry for detection of Raman spectrum with the resolution of 1 cm^{-1}. The excitation source was 532 nm line of He–Ne laser. The power of the Raman laser and its spot size were kept > 5 mW and ~ 1 µm respectively to avoid possible heating effect on the sample.

2.3 Field emission setup

The field emission current density versus applied electric field (J–E) and emission current versus time (I–t) characteristics were measured in a planar diode configuration in an all-metal ultra high vacuum (UHV) chamber evacuated to base pressure of 1×10^{-8} mbar. In a typical diode

configuration, a semi-transparent cathodoluminescent phosphor screen having diameter ~ 50 mm was held parallel to the cathode assembly. For powder synthesized material, the cathode is obtained by sprinkling very small quantity of the powder onto a piece of UHV compatible conducting carbon tape (~ 0.25 cm^2). This piece of carbon tape with sprinkled powder was pasted on copper rod connected to a linear motion drive, facilitating variation in cathode–anode separation. The FE measurements were carried out at a constant cathode–anode separation of 2 mm, the emission current was acquired on Keithley electrometer (6514) by varying the applied voltage between the cathode and anode with a step of 40 V (0–40 kV, Spellman, USA).

3 Results and discussion

3.1 X-ray diffraction (XRD) analysis

The X-ray diffraction (XRD) is widely used characterization technique for the study of structural investigation of synthesized materials via different methods. Figure 2 demonstrate the XRD pattern of as purchased TiO_2 powder [Curve (a)], as-prepared TiO_2 [Curve (b)] and soaked TiO_2 [Curve(c)] powder synthesized by solvothermal method. The presence of multiple diffraction planes in all XRD pattern indicates their polycrystalline nature. From curve (a) major

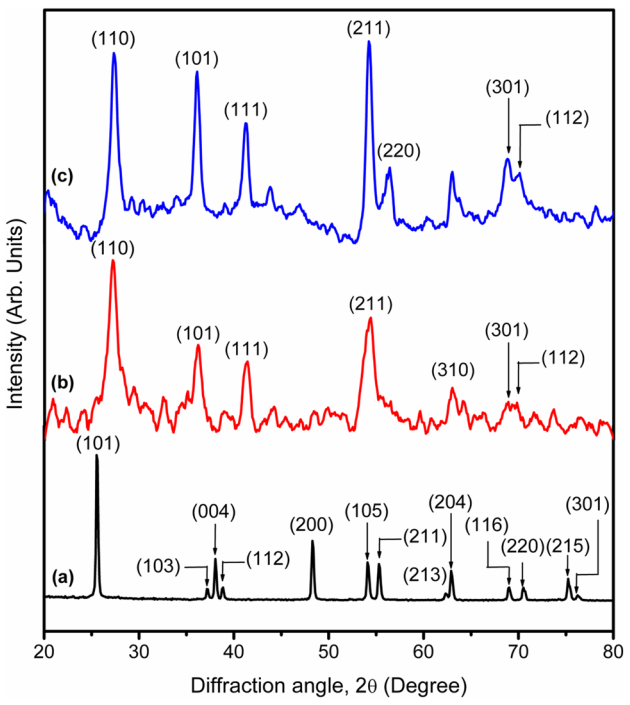

Fig. 2 X-ray diffraction (XRD) pattern of as purchased TiO_2 powder [Curve (a)], as-prepared TiO_2[Curve (b)] and soaked TiO_2 [Curve(c)] powder synthesized by solvothermal method

diffraction planes were observed at 2θ ~ 25.5°, 37.2°, 38.1°, 38.9°, 48.3°, 54.1°, 55.3°, 62.3°, 62.9°, 69.0°, 70.5°, 75.2° and 76.2° corresponding to (101), (103), (004), (112), (200), (105), (211) (213), (204), (116), (220), (215) and (301) diffraction planes corresponding to anatase phase of TiO_2 [JCPDS data card # 00-004-0477]. In curves (b) and (c) the major diffraction peaks were observed at 2θ ~ 27.4°, 36.2°, 41.2°, 54.2°, 56.3°, 62.9°, 68.9° and 69.7° corresponding to (110), (101), (111), (211), (220), (310), (301) and (112) diffraction planes of tetragonal rutile phase of TiO_2 [JCPDS data card # 00-021-1276]. No other impurity phases were observed in the XRD pattern. These results indicate the formation of pure rutile-TiO_2 using a facile and simple solvothermal method from its anatase phase. It is interesting to note that the preferred orientation of crystallites for as-prepared rutile-TiO_2 is along (110) and for soaked rutile-TiO_2 is (211). Applying Scherrer's equation we have calculated the average crystallite size (d) for as-prepared and soaked rutile-TiO_2 samples [38].

$$d_{x\text{-ray}} = \frac{0.9\lambda}{\beta \cos \theta_B} \tag{4}$$

where λ is the wavelength of diffracted radiation ($Cu_{K\alpha}$, λ = 1.54056 Å), θ_B is the Bragg angle and β is the full width at half maximum (FWHM) in radians. The calculated values of average crystallite size are found ~ 9.8 nm and ~ 18.7 nm for as-prepared and soaked rutile-TiO_2 samples respectively. Furthermore, the estimated lattice constants for the rutile-TiO_2 were found a ~ 0.47 nm and c ~ 0.29 nm respectively which are analogous with standard JCPDS data # 00-021-1276.

3.2 Micro-Raman spectroscopy analysis

Raman spectroscopy is widely employed for the study of chemical structure and the characteristic molecular vibration by interaction of laser light with the material. Figure 3 shows Raman spectra of as purchased TiO_2 powder [curve (a)], as-prepared TiO_2 [curve (b)] and soaked TiO_2 [curve(c)] powder in the scale 50–650 cm^{-1} synthesized by solvothermal method. As seen from curve (a) the Raman spectra shows a strong shoulder at ~ 141 cm^{-1} and three weak shoulders at ~ 394 cm^{-1}, ~ 514 cm^{-1} and ~ 637 cm^{-1} which are characteristics bands observed for anatase phase of TiO_2 [39]. The Raman spectra for curve(b) and (c) shows four Raman active bands at ~ 112 cm^{-1} (weak), ~ 241 cm^{-1} (weak), ~ 435 cm^{-1} (strong) and ~ 604 cm^{-1} (weak) associated with rutile phase of TiO_2 [40]. The Raman peaks at 112 cm^{-1} is for the mode of B_{1g} symmetry, 241 cm^{-1} is for second order scattering, 435 cm^{-1} is for E_g mode while 604 cm^{-1} is for A_{1g} mode [41]. The E_g mode is mainly due to the symmetric stretching vibration of O–Ti–O, the B_{1g} Raman active mode corresponds to symmetric bending vibration of O–Ti–O and

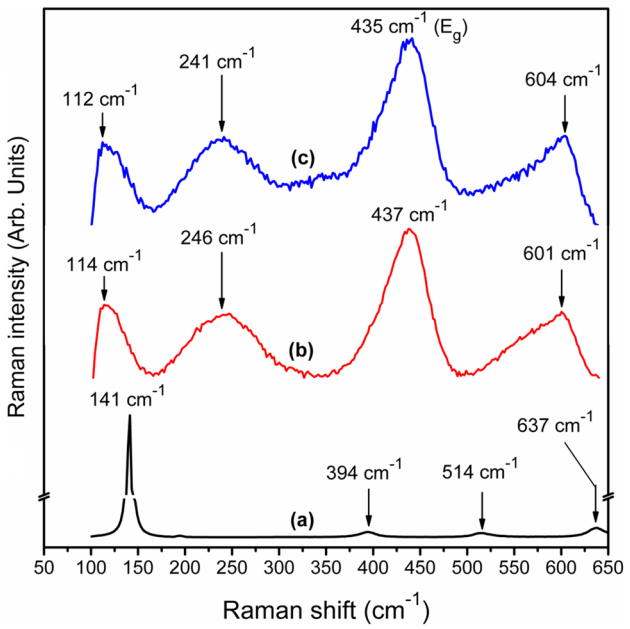

Fig. 3 Raman spectra of as purchased TiO_2 powder [Curve (a)], as-prepared TiO_2 [Curve (b)] and soaked TiO_2 [Curve(c)] powder

A_{1g} Raman active mode corresponds to the anti-symmetric bending vibration of O–Ti–O in rutile-TiO_2. No additional peaks were found in the both acquired Raman spectra suggesting the formation of pure rutile-TiO_2 phase in the present work. The intensity ratio between Raman vibrational modes (A_{1g}/E_g) for as-prepared and soaked rutile-TiO_2 were found quite similar (0.45 and 0.47) indicating the good degree of crystallinity of TiO_2 and the percentages of specific facets in as-prepared and soaked rutile-TiO_2 do not change during the soaking process [42].

3.3 Field emission scanning electron microscopy (FE-SEM) analysis

To investigate the surface morphology of as-prepared and soaked rutile-TiO_2 the field emission scanning electron microscopy (FE-SEM) was used. Figure 4 shows the FE-SEM images of as-prepared and soaked rutile-TiO_2 at ×100,000 and ×300,000 magnifications. Before imaging, the samples were coated with platinum by sputter method. From Fig. 4 it is clear that both as-prepared and soaked rutile-TiO_2 sample are dense and homogeneous. We observed from the FE-SEM micrographs, the soaking invokes a distinct change in surface morphology. The FE-SEM micrograph of as-prepared rutile-TiO_2 clearly shows randomly distributed nano-rods with tips like morphology with substantial polydispersity in terms of their width and length (Fig. 4a1 and a2). The average length is ~ 100 nm and diameter is ~ 22 nm. The FE-SEM micrograph of rutile-TiO_2 sample after soaking treatment under controlled pH ~ 7 shows nano-flowers like morphology composed of sharp needle tips having average size ~ 200 nm (Fig. 4b1 and b2). Thus, upon soaking treatment under controlled pH ~ 7 the surface morphology of rutile-TiO_2 changes from nano-rods with needle like tips morphology to nano-flowers. The change in surface morphology of rutile-TiO_2 upon soaking may be due to the agglomeration of nano-rods in mother liquor at pH ~ 7.

Figure 4a3 and b3 shows the EDX spectra for as-prepared and soaked rutile-TiO_2 respectively. The quantitative data analysis from the EDX spectra revealed that elemental composition for as-prepared rutile-TiO_2 is Ti ~ 24 at.% and O is ~ 76 at.% whereas for soaked rutile-TiO_2 is Ti ~ 20 at.% and O is ~ 80 in at.%. These results indicate the formation of oxygen rich rutile-TiO_2 after soaking by solvothermal method. These results are analogous with XRD (see Fig. 2) and Raman spectroscopy analysis (see Fig. 3).

3.4 Transmission electron microscopy (TEM) analysis

Formation of nano-rods with needle like tips morphology for as-prepared rutile-TiO_2 and nano-flowers like morphology for soaked rutile-TiO_2 was confirmed from transmission electron microscopy (TEM). Figure 5 shows TEM and HR-TEM micrographs of as-prepared and soaked rutile-TiO_2. The TEM image in Fig. 5a1 shows that the as-prepared rutile-TiO_2 is having randomly dispersed nano-rods with edged needles. The inset of Fig. 5a1 shows its selected area electron diffraction (SAED) pattern. The circular rings of bright spots in the SAED pattern indicate the polycrystalline nature of synthesized samples with high degree of crystallinity. Figure 5a2 is HR-TEM image of as-prepared rutile-TiO_2 sample. The magnified view of marked area of A in Fig. 5a2 shows that the inte-planar spacing between two adjacent lattice planes is ~ 0.34 nm, which is consistent with the spacing of (110) plane of rutile-TiO_2 [43]. Figure 5b1 shows TEM and Fig. 5b2 shows HR-TEM image of soaked rutile-TiO_2. As seen from the Fig. 5b1 after the soaking treatment the nano-rods with edged needles topography of TiO_2 changes in to nano-flowers having atomically sharp edges. These atomically sharp edges act as possible emission sites in field emission due enhancement in the local field. The circular rings of bright spots in the SAED pattern (Inset of Fig. 5b1) indicates the existence of high degree of crystallinity after soaking treatment. However, after soaking treatment a slight increase in distance between the adjacent lattice planes (~ 0.35 nm) has been observed.

3.5 UV–Visible spectroscopy analysis

Optical properties of as-prepared and soaked rutile-TiO_2 nano-structures were studied by using diffuse reflectance spectroscopy (DRS). Figure6 a and b display the

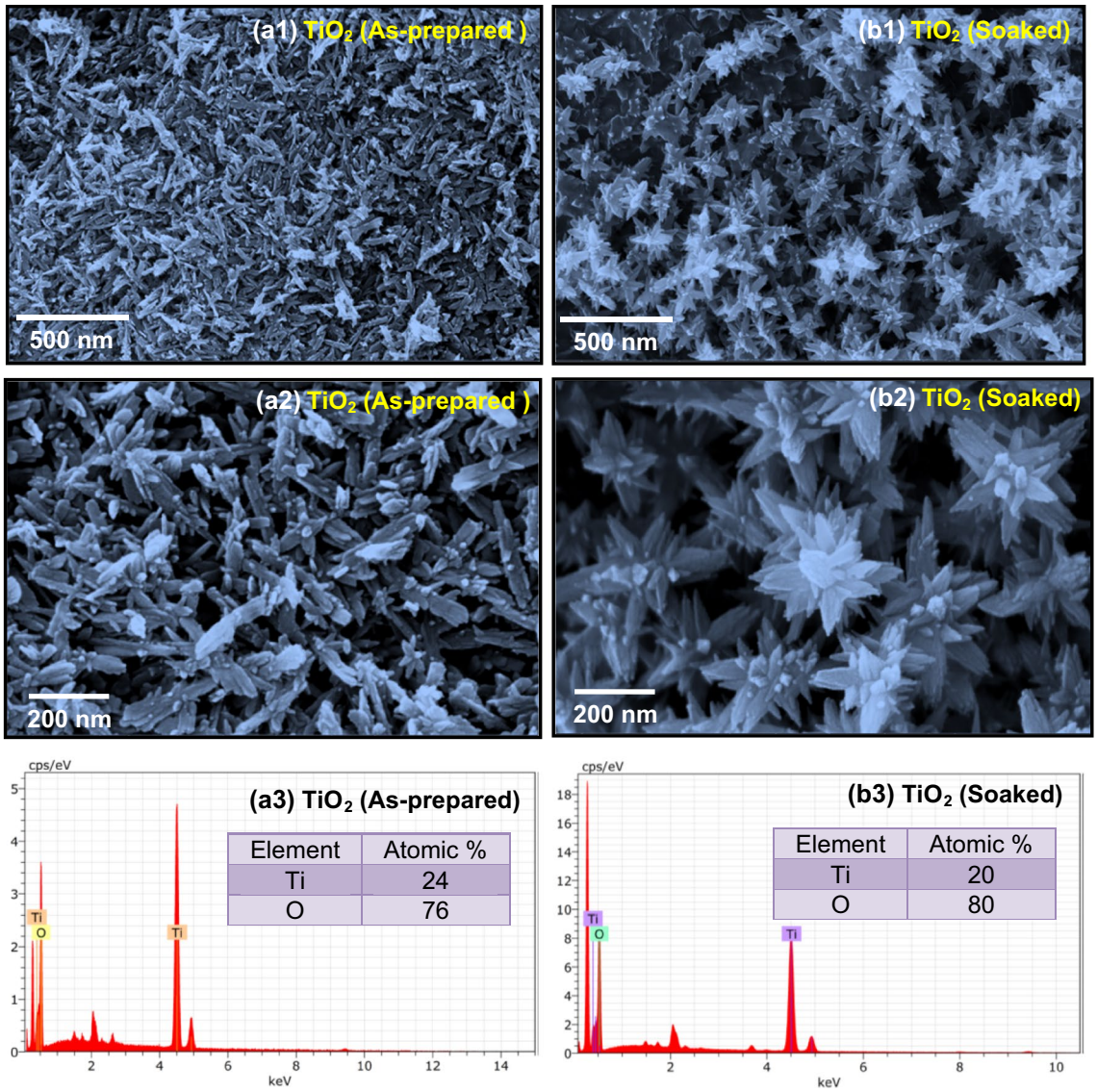

Fig. 4 Field emission scanning electron microscopy (FE-SEM) images of **a1** and **a2** as-prepared rutile-TiO_2, **b1** and **b2** soaked rutile TiO_2, EDXA spectra for **a3** as-prepared and **b3** soaked rutile-TiO_2 respectively

UV-Visible reflectance spectra of as-prepared and soaked rutile-TiO_2 nano-structures respectively. As seen both as-prepared and soaked rutile-TiO_2 nano-structures have absorption edge in the visible range. To order to estimate band gap of as-prepared and soaked rutile-TiO_2 nano-structures the reflectance (R) values has been converted to equivalent remission extinction coefficient, F(R) by using Kubelka–Munk transformation theory [44].

$$F(R) = \frac{(1-R)^2}{2R} \tag{5}$$

The inset of Fig. 6a and b display the generated Tauc's plot used for the computation of direct band gap using Kubelka–Munk transformation theory for as-prepared and soaked rutile-TiO_2 nano-structures respectively. It has been observed that the estimated optical band gap values for as-prepared and soaked rutile-TiO_2 nano-structures was ~ 3.04–3.15 eV which matches with reported values of band gap for rutile-TiO_2 in the literature [45].

3.6 Field emission analysis

High aspect ratio, sharp tip features, good stability and oxidation resistance are prerequisites to enhance the field emission (FE) properties of metal oxides. Among the various metal-oxides, TiO_2 is one of the most fascinating functional materials which have received considerable attention after

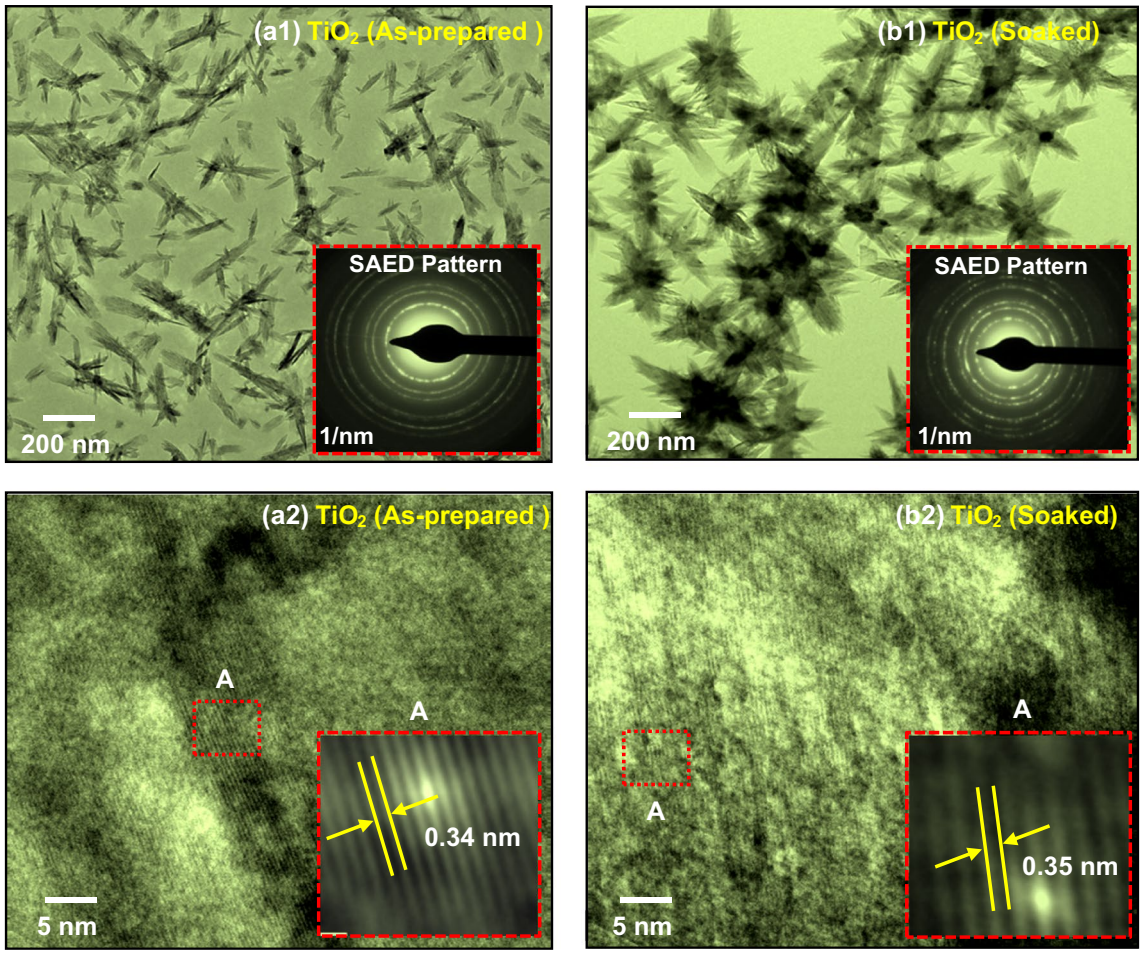

Fig. 5 Transmission electron microscopy (TEM) imagesof **a1** as-prepared rutile-TiO_2. The inset shows its selected area electron diffraction (SAED) pattern, **a2** HRTEM image for as-prepared rutile-TiO_2. The inset is the enlarged view of area 'A' of HR-TEM image, **b1** Soaked rutile-TiO_2. The inset shows its selected area electron diffraction (SAED) pattern and **b2** HRTEM image for soaked rutile-TiO_2. The inset is the enlarged view of area 'A' of HR-TEM image

carbon nanotubes for FE properties such as geometrical similarity of TiO_2 nanotubes [46], nanotubes with sharp tips [47], low work function (0.5 eV) [48], high packing density [49] etc. Furthermore, being a natural oxide, TiO_2 is not affected by the oxygen, so its exposure to O_2 will not affect its properties. Thus, no special measures need to be taken to prevent their reaction with air [50]. Its good electrical contact with substrate makes them suitable as electron per collation pathways for free electron transfer between interfaces [51].

The field emission (FE) properties of as prepared and soaked rutile TiO_2 field emitter were measured in a planar diode configuration in an all-metal ultra-high vacuum (UHV) system [52]. The field emission properties of as-prepared and soaked rutile-TiO_2 nano-structures are shown in Fig. 7. Figure 7a represents the variation of emission current density with applied electric field (J–E) characteristics of as-prepared and soaked rutile-TiO_2nano-structures. Here, the applied electric field given by, E = V/d, where V is the applied dc voltage and d is the cathode and anode separation. The emission current density is estimated as, J = I/A, where I is the emission current and A is the actual area of the emitter surface. From the figure it is clear that upon applied electric field the emission current increases exponentially according to Fowler–Nordheim (F–N) theory [53]. The turn-on field (E_{On}) for both as-prepared and soaked-TiO_2 is 4.8 V/μm at current density of 10 μA/cm^2. The observed turn-on field values for as-prepared and soaked-TiO_2 nano-structures are much smaller than the previously reported hierarchical TiO_2 nano-structures. A comparison between them is listed in Table 1.

The low turn-on field value for the as-prepared and soaked-TiO_2 nanostructures can attribute to the occurrence of atomically sharp edges of nano-rods and nano-flowers. The FE-SEM [Fig. 4] and TEM [Fig. 5] analysis further support this. Maximum emission current density of ~444 μA/cm^2has

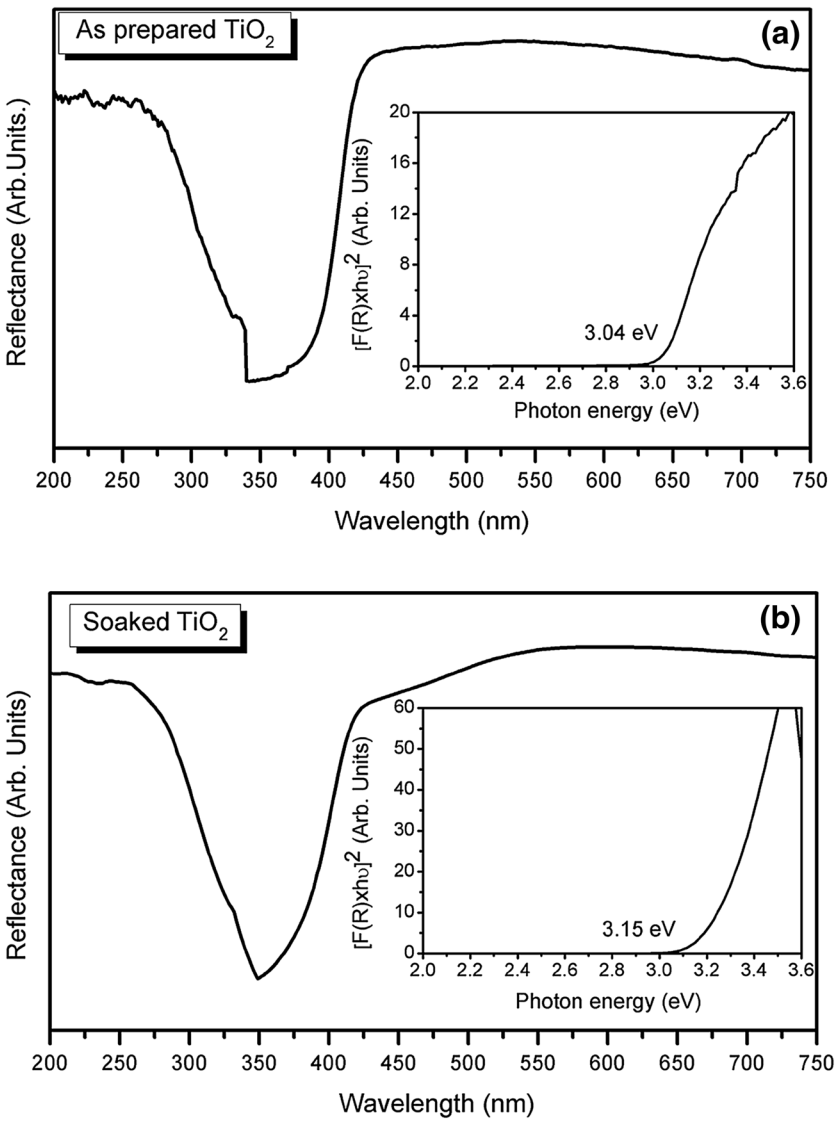

Fig. 6 UV–Visible DRS spectra of **a** As-prepared rutile TiO_2, **b** Soaked rutile TiO_2. The insets of figure a and b shows typical Tauc's plot used for the estimation of band gap using Kubelka–Munk transformation for as-preparedand soaked rutile-TiO_2 respectively

been drawn at applied field (E_{Th}) of 7.0 V/μm for as-prepared rutile-TiO_2based emitter compared to ~ 508 μA/cm^2 for soaked rutile-TiO_2 based emitter at applied field of 6.0 V/μm. The observed J–E characteristic further is analyzed by plotting a graph of ln(J/E^2) versus (1/E) known as the Fowler–Nordheim (F–N) plot. Figure 7b shows the F–N plot for as-prepared and soaked rutile-TiO_2nano-structures. The nonlinear behaviour over the entire scale of the applied electric field indicates semiconductor nature of as-prepared and soaked rutile-TiO_2 nano-structured emitter material. The stability of field emission current is one of the important parameters in cold cathodes for its practical applications. Figure 7c and 7d shows the relation between the emission current as a function of time (I–t plot) for as-prepared and soaked rutile-TiO_2nano-structures respectively. These plots corresponding to the preset values of 1.0 μA for both as-prepared and soaked rutile-TiO_2, recorded at a base pressure of 1×10^{-8} mbar with sampling time of 30 s for more than 3 h and 15 min. duration. As seen the emitter current remains constant in the range 0.5–1.5 μA for as-prepared rutile-TiO_2 sample and in the range 0.75–2.5 μA for soaked rutile-TiO_2 sample respectively. However some fluctuations/spikes were observed in the I–t plots. This fluctuations/spike appearance in the measured emission current may be due to adsorption/desorption, migration and also due to the ion bombardment of the residual gas atoms/molecules on the emitter surface due to applied electric field. These processes occur on the atomic/molecular level which leads to an instantaneous change in the local work function at the possible emission site [59]. However, it seems that the average emission current quite stable over the entire duration. Both as-prepared and soaked rutile-TiO_2 emitters exhibit stable field emission behaviour with average current fluctuation within ±4–5%. It indicates good physical and chemical stability of both as-prepared and soaked rutile-TiO_2emitters. The field emission images are

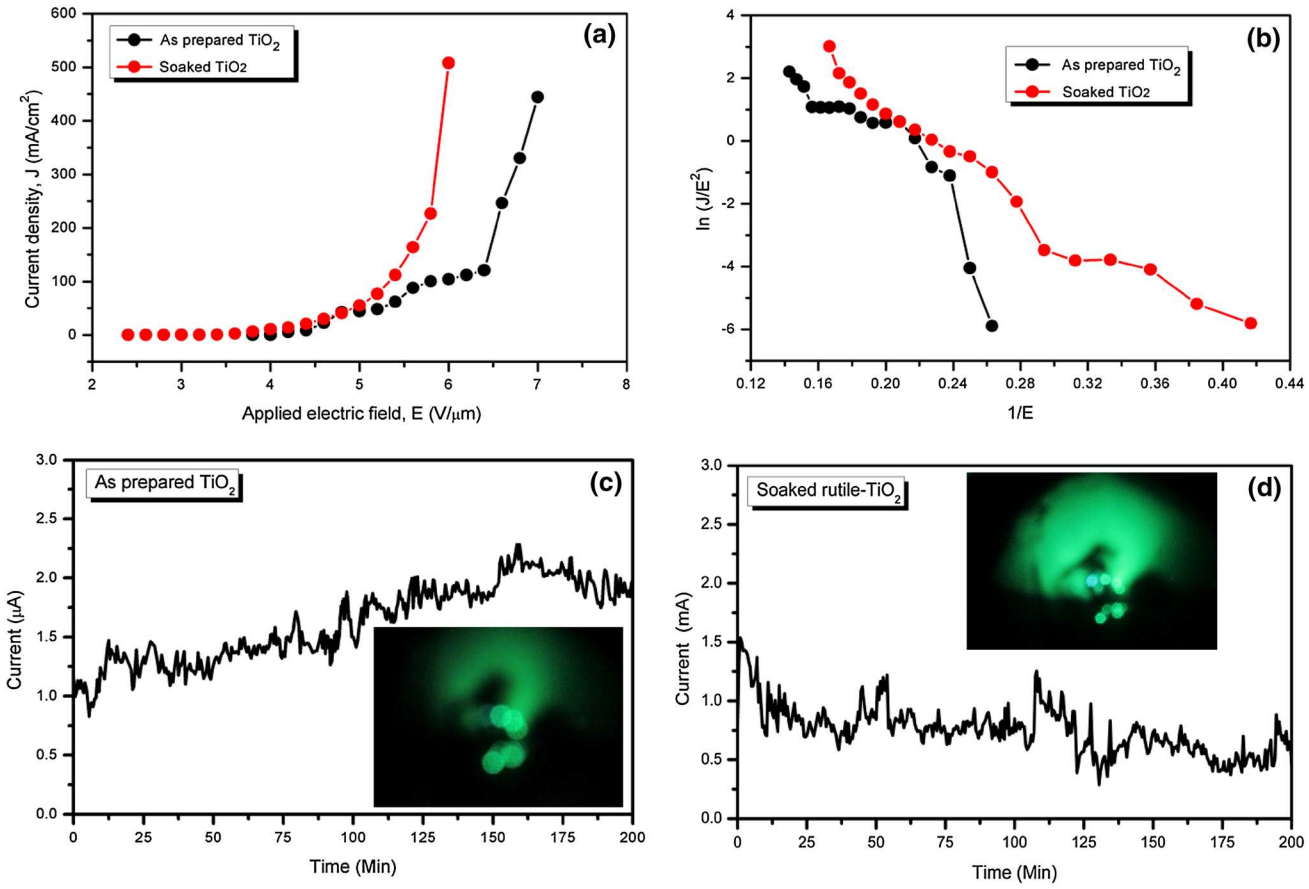

Fig. 7 Field emission investigation of rutile-TiO_2 nano-structures **a** Applied electrical field as a function of emission current density, **b** F–N plot showing non-linear behaviour typical of quantum mechanical tunnelling **c** Emission current as a function of time (I–t plot) for as-prepared rutile-TiO_2 and **d** Emission current as a function of time (I–t plot) for soaked rutile-TiO_2. Inset of figure c and d shows field emission images for as-prepared and soaked rutile-TiO_2 emitters respectively

Table 1 Comparison of turn-on field values of as-prepared and soaked-TiO_2 nano-structures with previously reported hierarchical TiO_2 nano-structures

Morphology	Synthesis route	E_{On}(V/μm)@ 10 μA/cm^2	Ref.
TiO_2 Nano-wires/nano-tubes	Hydrothermal	6.7/7.5	[54]
TiO_2 nano-wires	Thermal evaporation	5.7	[55]
TiO_2 nano-tubes	Anodization	11.2	[56]
TiO_2 nano-tips	Anodization	8.6	[57]
TiO_2 nano-tube arrays	Liquid phase reduction	11.86	[58]
TiO_2 nano-rods/nano-flowers	Hydrothermal	4.8	Present

shown in the inset of Fig. 7c and d for as-prepared and soaked rutile-TiO_2emitters respectively. The images depict tiny bright spots, corresponding to the emission from the most protruding part on the emitter surface. These images clearly show that the density of emission spots for the soaked rutile-TiO_2 emitter is higher than as-prepared rutile-TiO_2 emitter. The increase in the local field may be due to high density of atomically needle like sharp edges in nano-flower structured soaked rutile-TiO_2 because they acts as potential emission sites. The SEM and TEM analysis further supports this (see Figs. 4, 5).

4 Conclusions

In present work we report synthesis of rutile-TiO_2 from anatase-TiO_2 by using a simple Solvothermal method. The formation of single phase rutile-TiO_2 has been confirmed by

X-ray diffraction (XRD) and Raman spectroscopy analysis. The XRD analysis revealed that as-prepared and soaked-TiO_2 has pure rutile phase with tetragonal crystal structure. The field emission scanning electron microscopy (FE-SEM) shows that as-prepared TiO_2 has nano-rods like morphology whereas soaked-TiO_2 has nano-flowers like morphology with atomically sharp edges. Similar results were confirmed by high resolution transmission electron microscopy (HR-TEM) analysis. The UV–Visible spectroscopy analysis showed that as-prepared and soaked rutile-TiO_2nano-structures have absorption edge in the visible range. The optical band gap estimated for both as-prepared and soaked-TiO_2 was found ~ 3.04–3.15 eV. Finally, field emission properties of as-prepared and soaked rutile-TiO_2 nano-structures were investigated. It has been observed that as-synthesized and soaked rutile-TiO_2 display excellent field emission properties with low turn-on field (~ 4.8 V/μm for 10 μA/cm^2), maximum current density [~ 444 μA/cm^2 (as-prepared) and 508 μA/cm^2 (soaked)] and superior current stability (~ 3 h for ~ 1 μA). Thus, the obtained results demonstrate that the rutile-TiO_2 nanostructures can be used for practical applications in vacuum nano/microelectronic devices.

Acknowledgements Ajinkya Bhorde thankful to Department of Science and Technology (DST), Government of India for INSPIRE Ph. D. fellowship. Ravindra waykar, Shruthi Nair and Subhash Pandharkar are thankful to the and Ministry of New and Renewable Energy (MNRE), Government of India for the financial support under National Renewable Energy Fellowship (NREF) program. Haribhau Borate is thankful to University Grants Commission, New Delhi for financial support under Faculty Improvement Program (FIP) for college teachers. One of the authors Sandesh Jadkar is thankful to University Grants Commission (UPE program), New Delhi and Indo-French Centre for the Promotion of Advanced Research-CEFIPRA, Department of Science and Technology, New Delhi for special financial support.

References

1. W. Guo, T. Liu, L. Huang, Mater. Lett. **65**, 3384 (2011)
2. X. Fang, J. Yan, L. Hu, H. Liu, P. Lee, Adv. Funct. Mater. **22**, 1613 (2012)
3. L. You, Y. Sun, J. Ma, Y. Guan, Sens. Actuators B **157**, 401 (2011)
4. L. Li, N. Koshizaki, J. Mater. Chem. **20**, 2972–2978 (2010)
5. B. Liu, E. Aydil, J. Am. Chem. Soc. **131**, 3985 (2009)
6. V. Subramanian, E.W. Eduardo, V.K. Prashant, J. Am. Chem. Soc. **126**, 4943 (2004)
7. T. Kandiel, A. Feldhoff, L. Robben, R. Dillert, D. Bahnemann, Chem. Mater. **22**, 2050 (2010)
8. R. Patil, R. Devan, Y. Liou, Y. Ma, Sol. Energy Mater. Sol. Cells **147**, 240 (2016)
9. R. Devan, Y. Ma, R. Patil, L. Schmidt-Mende, RSC Adv. **6**, 62218 (2016)
10. C. Kim, R. Buonsanti, R. Yaylian, D. Milliron, J. Cabana, Adv. Energy Mater. **3**, 1286 (2013)
11. J. Gong, Y. Li, Z. Hu, Z. Zhou, J. Phys. Chem. C .**114**, 9970 (2010)
12. T. Ochiai, A. Fujishima, J. Photochem. Photobiol. C **13**, 247 (2012)
13. Y. Lu, H. Yu, S. Chen, X. Quan, H. Zhao, Environ. Sci. Technol. **46**, 1724 (2012)
14. T. Zheng, Z. Tian, B. Su, Z. Lei, Ind. Eng. Chem. Res. **51**, 1391 (2012)
15. P. Singh, N. Jadhav, Int. J. Electroact. Mater. **3**, 1–5 (2015)
16. G. Wilson, A. Matijasevich, D. Mitchell, J. Schulz, G. Will, Langmuir **22**, 2016 (2006)
17. N. Khatun, S. Tiwari, C. Vinod, C. Tseng, S. Liu, S. Biring, S. Sen, J. Appl. Phys. **123**, 245702 (2018)
18. Z. Ding, X. Hu, G. Lu, P. Yue, Langmuir. **16**, 6216 (2000)
19. S. Muduli, W. Lee, V. Dhas, Appl. Mater. Interfaces **1**(9), 2030 (2009)
20. R. Almeida, A. Marques, J. Mater. Sci. Mater. Electron. **20**, 307 (2009)
21. H. Kim, J. Lee, N. Yantara, P. Boix, S. Kulkarni, S. Mhaisalkar, M. Gratzel, N. Park, Nano Lett. **13**, 2412 (2013)
22. W. Junga, N. Kwaka, T. Hwanga, K. Yi, Appl. Surf. Sci. **261**, 343 (2012)
23. Y. Zhu, H. Li, Y. Koltypin, Y.R. Hacohen, A. Gedanken, Chem. Commun. **24**, 2616–2617 (2001)
24. G. Wang, G. Li, Eur. J. Phys. D **24**, 355 (2003)
25. A. Liao, C. Wang, J. Chen, X. Zhang, Y. Li, J. Wang, Mater. Res. Bull. **70**, 988 (2015)
26. N. Asim, S. Ahmadi, M. Alghoul, F. Hammadi, K. Saeedfar, K. Sopian, Int. J. Photoenergy **21**, 518156 (2014)
27. W. Li, C. Ni, H. Lin, C. Huang, S. Shah, J. Appl. Phys. **96**, 6663 (2004)
28. N. Jagtap, M. Bhagwat, P. Awati, V. Ramaswamy, Thermochim. Acta **37**, 427 (2005)
29. D. Hanaor, C. Sorrell, J. Mater. Sci. **46**, 855 (2011)
30. M. Zavala, S. Morales, M. Santos, Heliyon, **3**,00456 (2017)
31. C. Brinker, G. Scherer, S.-G. Science, *The physics and chemistry of Sol–Gel processing* (Academic Press Inc., USA, 1990)
32. B. Wang, D. Xue, Y. Shi, F. Xue, Titania 1D nanostructured materials: synthesis, properties and applications, In *Nanorods, nanotubes and nanomaterials research progress*, ed. by W. Prescott, A. Schwartz (New Nova Science Publishers Inc., New York, 2008), pp. 163–201
33. Y. Wang, G. Hu, X. Duan, H. Sun, Q. Xue, Chem. Phy. Lett. **365**, 427 (2002)
34. R. Shannon, J. Pask, J. Am. Ceram. Soc. **48**, 391 (1965)
35. M. Finnegan, H. Zhang, J. Banfield, Chem. Mater. **20**, 3443 (2008)
36. F. Meldrum, H. Colfen, Chem. Rev. **108**, 4332 (2008)
37. M. Wu, G. Lin, D. Chen, G. Wang, D. He, S. Feng, R. Xu, Chem. Mater. **14**, 1974 (2002)
38. B. Cullity, S. Stock, *Elements of X-ray Diffraction*, 3rd ed. (Princeton Hall, New Jersey, 2001)
39. Y. Xing, S. Wang, B. Fang, G. Song, D. Wilkinson, S. Zhang, J. Power Sources **385**, 10 (2018)
40. Y. Yoon, J. Park, Nanotechnology **29**, 165705 (2018)
41. G. Chen, J. Chen, Z. Song, C. Srinivasakannan, J. Peng, J. Alloys Compd. **585**, 75 (2014)
42. J. Yan, G. Wu, N. Guan, L. Li, Z. Li, X. Cao, Phys.Chem. Chem. Phys. **15**, 10978 (2013)
43. Y. Baoa, Q. Kang, C. Jian, Z. Ma, Mater. Lett. **214**, 272 (2018)
44. M. Patel, A. Chavada, I. Mukhopadhyay, J. Kim, A. Ray, Nanoscale **8**, 2293 (2016)
45. N. Khatun, P. Anita, D. Rajput, S. Bhattacharya, S. Jha, S. Brining, S. Sen, Ceram. Int. **43**, 14128 (2017)
46. R. Devan, Y. Ma, M. More, R. Khare, V. Antad, R. Patil, V. Thakare, R. Dhayal, L. Mendeg, RSC Adv. **6**, 98722 (2016)
47. J. Liang, G.M. Zhang, ACS Appl. Mater. Interfaces **4**, 6053 (2012)
48. G. Rothenberger, D. Fitzmaurice, M. Graetzel, J. Phys. Chem. **96**, 5983 (1992)
49. A. Datta, P. Chavan, F. Sheini, M. More, D. Joag, A. Patra, Cryst. Growth Des. **9**, 4157 (2009)

50. Y. Alivov, S. Molloi, J. Appl. Phys. **108**, 024303 (2010)
51. J. Chen, C. Wang, B. Ma, Y. Li, J. Wang, R. Guo, W. Liu, Thin Solid Films **517**, 4390 (2009)
52. P. Bankar, M. Pawar, A. Pawbake, S. Warule, D. Late, M. More, RSC Adv. **6**, 95092 (2016)
53. P. Chikate, P. Bankar, Y. Ma, S. Patil, M. More, D. Phase, P. Shirage, R. Devan, RSC Adv. **8**, 21664 (2018)
54. M. Choi, Z. Zhang, J. Chen, Z. Deng, K. Yong, RSC Adv. **5**, 19470 (2015)
55. J. Wu, H. Shih, W. Wu, Chem. Phys. Lett. **413**, 490 (2005)
56. G. Liu, F. Li, G. Lu, D. Wang, D. Tang, C. Liu, X. Ma, H. Cheng, Nanotechnology **19**, 025606 (2008)
57. H. Pan, X. Qiu, I. Ivanov, H. Meyer, W. Wang, W. Zhu, M. Paranthaman, Z. Zhang, G. Eres, B. Gu, Appl. Catal. B **93**, 90 (2009)
58. C. Wang, J. Chen, L. Wang, Y. Kang, D. Li, F. Zhou, Thin Solid Films **520**, 5036 (2012)
59. S. Suryawanshi, S. Warule, S. Patil, K. Patil, M. More, ACS Appl. Mater. Interfaces **6**, 2018 (2014)